

Numerical Simulation of CO₂ Leakage from a Geologic Disposal Reservoir, Including Transitions from Super- to Sub-Critical Conditions, and Boiling of Liquid CO₂

Karsten Pruess

Earth Sciences Division, Lawrence Berkeley National Laboratory, Berkeley, CA 94720

Abstract

The critical point of CO₂ is at temperature and pressure conditions of $T_{\text{crit}} = 31.04\text{ }^{\circ}\text{C}$, $P_{\text{crit}} = 73.82$ bar. At lower (subcritical) temperatures and/or pressures, CO₂ can exist in two different phase states, a liquid and a gaseous state, as well as in two-phase mixtures of these states. Disposal of CO₂ into brine formations would be made at supercritical pressures. However, CO₂ escaping from the storage reservoir may migrate upwards towards regions with lower temperatures and pressures, where CO₂ would be in subcritical conditions. An assessment of the fate of leaking CO₂ requires a capability to model not only supercritical but also subcritical CO₂, as well as phase changes between liquid and gaseous CO₂ in sub-critical conditions. We have developed a methodology for numerically simulating the behavior of water-CO₂ mixtures in permeable media under conditions that may include liquid, gaseous, and supercritical CO₂. This has been applied to simulations of leakage from a deep storage reservoir in which a rising CO₂ plume undergoes transitions from supercritical to subcritical conditions. We find strong cooling effects when liquid CO₂ rises to elevations where it begins to boil and evolve a gaseous CO₂ phase. A three-phase zone forms (aqueous - liquid - gas), which over time becomes several hundred meters thick as decreasing temperatures permit liquid CO₂ to advance to shallower elevations. Fluid mobilities are reduced in the three-phase region from phase interference effects. This impedes CO₂ upflow, causes the plume to spread out laterally, and gives rise to dispersed CO₂ discharge at the land surface. Our simulation suggests that temperatures along a CO₂ leakage path may decline to levels low enough so that solid water ice and CO₂ hydrate phases may be formed.

1. Introduction

Combustion of fossil fuels such as oil, natural gas, and coal currently generates in excess of 27 billion tonnes of carbon dioxide (CO₂) per year worldwide (DOE, 1999), virtually all of which is discharged into the earth's atmosphere. Because of the expanded use of fossil fuels, the atmospheric concentration of CO₂ has risen from preindustrial levels of 280 ppm (parts per million) to present day values of approximately 365 ppm (Keeling and Whorf, 1998). The Intergovernmental Panel on Climate Change (IPCC) has projected that for a "business as usual" energy scenario the atmospheric concentrations of CO₂ may double by the middle of the 21st century, and may continue to rise at increasing rates beyond (IPCC, 1996). Atmospheric CO₂ is a "greenhouse gas," so-called because it traps outgoing infrared and thermal radiation, thereby increasing near-surface temperatures. There is some evidence from climate modeling that increased atmospheric concentrations of CO₂ may be the chief contributor to "global warming," currently estimated at 0.3 - 0.6 °C during the last 150 years (Ledley et al., 1999).

The U.S. Department of Energy (DOE) and other organizations have initiated broad technology programs to assess and develop methods for reducing atmospheric emissions of CO₂ (DOE, 1999). One of the more promising concepts involves disposal of CO₂ into geologic formations, including oil and gas reservoirs, unmineable coal beds, and saline aquifers. CO₂ disposal into oil and gas reservoirs, and coal beds, may offer collateral benefits in terms of enhanced recovery of oil and natural gas. Saline aquifers are attractive as CO₂ disposal reservoirs because they are generally unused and offer potentially large storage capacity. At the Sleipner Vest field in the Norwegian sector of the North Sea, a CO₂ disposal project has operated since August 1996, successfully injecting approximately 1 million tonnes of CO₂ per year into an aquifer with 3.2 wt.-% salinity and initial fluid pressures of approximately 110 bar (Korbøl and Kaddour, 1995; Kongsjorden et al., 1997; Holloway, 1997; Zweigel and Gale, 2000; Lindeberg et al., 2001; Torp and Gale, 2002).

There is a general consensus in the technical community that geologic disposal of CO₂ into saline aquifers would be made at supercritical pressures (Holloway and Savage, 1993; Hitchon et al., 1999). The critical point of CO₂ is at temperature and pressure conditions of $T_{\text{crit}} = 31.04\text{ }^{\circ}\text{C}$, $P_{\text{crit}} = 73.82\text{ bar}$ (Vargaftik, 1975). At lower (subcritical) temperatures and/or pressures, CO₂ can exist in two different phases, a liquid and a gaseous state, as well as two-phase mixtures of these states (Fig. 1.1). Supercritical CO₂ forms a phase that is distinct from the aqueous phase and can change continuously into either gaseous or liquid CO₂ with no phase boundaries. CO₂ leaking from a disposal reservoir could flow upward towards regions with lower temperatures and pressures, where CO₂ would be in subcritical conditions. An assessment of potential leakage

behavior requires a capability to model not only supercritical CO₂, but also subcritical CO₂, as well as phase changes between liquid and gaseous CO₂. This paper introduces a methodology for numerically simulating the behavior of water-CO₂ mixtures in permeable media under conditions that may include all different phase compositions.

The thermodynamic issues relevant to upflow of CO₂ from a deep storage reservoir are illustrated in Fig. 1.2 which shows the saturation pressure of CO₂ as a function of temperature in the range of interest for CO₂ disposal into brine formations. Here and throughout the paper, thermophysical properties of CO₂ were calculated within experimental accuracy from the correlations of Altunin (1975), using computer programs kindly provided to us by Victor Malkovsky of IGEM, Moscow (private communication, 1999). The saturation line ends at the critical point, here marked with a solid circle. Fig. 1.2 also shows two hydrostatic pressure profiles, calculated for a geothermal gradient of 30 °C per km, typical for continental crust, for two average land surface temperatures of 5 °C and 15 °C, respectively. Both profiles pass in the vicinity of the critical point of CO₂, and the one for 5° C surface temperature intersects the CO₂ saturation line, indicating that a bubble of CO₂ rising at nearly hydrostatic pressure would undergo a phase transition from liquid to gas at a pressure of approximately 63 bars, corresponding to a depth of approximately 630 m. Leakage of CO₂ from a deeper brine formation may cause some overpressure, which would shift the pressure profiles towards higher values. Phase change from liquid to gas is to be expected if CO₂ escapes upward at rates large enough so that not all of the leaking CO₂ can be retained as dissolved solute in the aqueous phase.

Phase change may have large effects on leakage rates, because CO₂ density is much lower for the gaseous than for the liquid state (Fig. 1.3). At subsurface (T, P) conditions, liquid CO₂ is always less dense than aqueous phase and thus is subject to upward buoyancy force. A transition to gaseous conditions would greatly enhance the buoyancy forces and could accelerate fluid leakage, as well as causing a rapid increase in fluid pressures at shallower horizons. This in turn could open pre-existing faults and fractures, enhancing their permeability and further increasing leakage rates. Reduced CO₂ solubility at the lower pressures prevailing at shallower depths would also come into play. It is of interest to determine whether these processes and effects can be self-enhancing to the point where they could cause a catastrophic, eruptive failure of a CO₂ disposal system (Chivas et al., 1987). Catastrophic releases of CO₂-rich gas with fatalities have occurred at two lakes in Cameroon, in 1984 at Lake Monoun (Sigurdsson et al., 1987), and in 1986 at nearby Lake Nyos (Tazieff, 1991). Pruess and García (2002) simulated the migration of CO₂ up a fault under supercritical conditions. Their simplified model showed that CO₂ discharge rates can increase over time, but this occurred in a gradual, bounded manner.

This paper presents a first exploratory study of CO₂ leakage under conditions that involve phase transitions from liquid to gaseous CO₂. As will be seen below, boiling of liquid CO₂ gives rise to large latent heat effects. Numerical simulation of flow processes with phase change requires coupled treatment of fluid flow and heat transfer. Our approach borrows from techniques developed in geothermal reservoir simulation (O'Sullivan et al., 1985; Battistelli et al., 1997), as implemented in the TOUGH2 numerical simulator (Pruess et al., 1999). TOUGH2 models flow processes with phase change through simultaneous solution of mass and energy balances. The continuum (field) equations are discretized in space and time, and the resulting system of non-linear algebraic equations is solved simultaneously for all primary thermodynamic variables of all grid blocks by Newtonian iteration. Preconditioned conjugate gradient methods are used to treat the linear equations arising at each iteration step (Moridis and Pruess, 1998). The adaptation of geothermal reservoir simulation techniques for modeling flows that involve brine and supercritical CO₂ was recently described by Pruess and García (2002), who also summarized the governing mass- and energy-balance equations. Here we extend these methods to account for all possible fluid phase combinations in water-CO₂ mixtures at conditions ranging from sub- to super-critical. We first present our treatment of fluid phase conditions, and then proceed to investigate CO₂ leakage behavior under conditions that involve an interplay of three fluid phases: a - aqueous, l - liquid CO₂, and g - gaseous CO₂.

2. Fluid Phase Conditions

The two-component system water-CO₂ may exist in any one of seven different phase combinations (Fig. 2.1): three single-phase states, three two-phase states, and a three-phase state. Representation of these phase conditions, and possible transitions between them, needs to address the following issues,

- accurate representation of thermophysical properties of water-CO₂ mixtures (density, viscosity, enthalpy, mutual solubility) in terms of appropriate primary thermodynamic variables (such as temperature, pressure, mass fractions of components, phase saturations);
- recognition of phase conditions and phase change (appearance or disappearance).

As had been mentioned above, the correlations of Altunin et al. (1975) are used in this paper to represent properties of CO₂ over a broad range of temperature and pressure conditions within experimental accuracy, except for narrow intervals around the critical point where larger errors occur. Water properties are likewise obtained within experimental accuracy from the steam table equations given by the International Formulation Committee (1967). Partitioning of water and CO₂ among different co-existing phases (mutual solubility) is calculated on the basis of local thermodynamic equilibrium, i.e., requiring chemical potentials of a component to be equal in

different phases. Certain approximations are made in the actual implementation of the chemical equilibrium constraints (Pruess and García, 2002). Brines are modeled as NaCl solutions, with proper dependence of density, viscosity, enthalpy, and vapor pressure of the aqueous phase on solute concentration (Battistelli et al., 1997). Effects of salinity on CO₂ solubility in the aqueous phase are described with an extended version of Henry's law (Pruess and García, 2002).

2.1 Interpolation from Tables

Within the context of numerical simulation of water-CO₂ mixtures, it is actually more convenient not to use the Altunin et al. (1975) correlations directly. Instead, we employ these correlations to generate CO₂ properties on a 2-D grid of temperature and pressure values, and then obtain parameters needed during the simulation by linear interpolation on this grid (Fig. 2.2). One advantage of this approach is that table lookup and interpolation are computationally much faster than calculating the full correlations, while providing excellent accuracy for a modest number of table points (of order of 100 each in the temperature and pressure domains). A practically more important advantage is that tabular data may be generated in a way that permits an easy recognition of all phase conditions for CO₂. This is accomplished by including grid points on the saturation line itself in the tabulation (Fig. 2.2). More specifically, we specify a sequence of sub-critical temperatures, calculate their saturation pressures $P_{\text{sat}}(T)$, and include these temperatures and pressures in the tabulation. The critical temperature and pressure are also included. Additional table points are generated for pressures lower than the smallest P_{sat} , for pressures larger than P_{crit} , and for temperatures larger than T_{crit} .

In practice we choose temperature and pressure intervals of order 1-2 °C and 2-5 bars, respectively, to achieve satisfactory accuracy for interpolation. The temperature-pressure grid shown in Fig. 2.2 is intentionally very coarse to clearly show the issues arising in interpolation. For two-phase gas-liquid conditions, thermophysical properties are obtained by 1-D interpolation along the saturation line, while for single-phase conditions 2-D interpolation is made in the appropriate temperature and pressure intervals. This scheme provides accurate thermophysical data for all phase conditions in a robust and efficient manner. The added presence of an aqueous phase adds only a minor complication, because conditions of interest for CO₂ disposal in brine formations involve modest (near-ambient) temperatures, with pressures mostly in the tens to hundreds of bars. Water saturation pressure is therefore a very small and essentially insignificant fraction of total fluid pressure.

Fig. 2.3 shows the specific enthalpy of gaseous and liquid CO₂ along the saturation line, as obtained by interpolation from our tabular equation of state. Away from the critical point, the latent

heat of vaporization amounts to several hundred kJ/kg, so that boiling of liquid CO₂ will require substantial heat transfer. Decompression of high-pressure CO₂ is accompanied by large increases in specific enthalpy for supercritical conditions as well (Fig. 2.4), so that migration of CO₂ to lower-pressure environments will produce cooling effects even when no phase change is involved.

2.2 Algorithms for Phase Transitions

Depending on fluid phase composition, different thermodynamic parameters may not be independent, and different sets of independent thermodynamic variables must be used (see Table 2.1). Single-phase conditions are characterized by pressure P and temperature T , and in addition require specification of the mass fraction X of CO₂ present in the fluid phase. In two-phase conditions, CO₂ mass fraction is no longer an independent variable, and we use either the aqueous phase saturation S_a or the saturation S_g of the gaseous CO₂-rich phase to define the thermodynamic state of the system. In two-phase conditions with an aqueous phase present, CO₂ partial pressure can be obtained from the primary variables as $P_{CO_2} = P - P_{sat,w}(T)$, where $P_{sat,w}$ is the saturated vapor pressure of water. CO₂ mass fraction can then be computed from (T, P_{CO_2}) . When only two CO₂-rich phases exist, water partial pressure can be obtained from the primary variables as $P_w = P - P_{sat,CO_2}(T)$, and mass fractions of components in phases can then be calculated. In three-phase conditions, temperature is not an independent variable but is implicitly determined from total pressure according to $P = P_{sat,CO_2}(T) + P_{sat,w}(T)$. Experience in geothermal reservoir simulation has proven variable switching in response to different phase conditions a very effective technique.

When salinity (NaCl) is included as a third mass component in addition to water and CO₂, an additional primary variable is needed, labeled “ X_{sm} ” in Table 2.1. This can be chosen as NaCl mass fraction dissolved in one of the fluid phases when no solid salt is present. For conditions with solid salt present, dissolved mass fractions are determined by thermodynamic equilibrium (solubility limit), and “solid saturation” S_s , the fraction of pore space containing solid salt, is used as a primary variable. In the latter case we may have as many as four active phases: three fluid phases, and solid precipitate. The simulations presented below do not include salinity.

The treatment outlined above was implemented in a fluid property module “EOSM” for the general-purpose reservoir simulation code TOUGH2 (Pruess et al., 1999). In most TOUGH2 modules, different phase compositions are distinguished by means of distinctive numerical ranges of the primary thermodynamic variables. For example, for single phase conditions the third primary variable X_3 denotes CO₂ mass fraction X (see Table 2.1), which has a possible numerical range between 0 and 1. Aqueous phase saturation S_a used as a primary variable in a-l and a-g two-phase

conditions has that same numerical range, but may be distinguished from X if by convention a number such as 10 is added, so that numerical values between 10 and 11 would indicate that X3 refers to aqueous phase saturation, with $S_a = X3 - 10$. A scheme of recognizing phase conditions from the numerical values of primary variables is very convenient for systems with a small number of different phase combinations. For a system with as many as seven different phase combinations as is considered here, however, it is better to use a numerical index to distinguish different phase compositions (Adenekan et al., 1993; Pruess and Battistelli, 2002), and this is the approach adopted here. Table 2.1 and Fig. 2.1 list the phase indices used to distinguish the different possible fluid phase compositions that may be present in a grid block.

Distinguishing phase compositions through indexing rather than through the numerical values of primary variables has additional advantages,

- (1) it avoids loss of accuracy from numerical cancellation that occurs when, e.g., a number 10 is added to phase saturations S in order to place them in a different numerical range than mass fractions X ;
- (2) initialization of phase conditions upon (dis-)appearance of a phase can be made in a more robust way, e.g. by specifying finite windows for phase (dis-)appearance rather than using a “hair trigger” criterion.

For example, in two-phase aqueous-gas conditions we need to determine whether a liquid phase can evolve to form a three-phase system. To do this we monitor CO_2 partial pressure, $P_{CO_2} = P - P_{sat,w}(T)$, where $P_{sat,w}$ is the saturated vapor pressure of water. From a thermodynamic viewpoint, a liquid phase will evolve when P_{CO_2} exceeds saturated CO_2 pressure P_{sat,CO_2} . However, our numerical experiments have shown that the criterion $P_{CO_2} > P_{sat,CO_2}$ for a transition to three-phase conditions may lead to very unstable behavior, where liquid phase may frequently appear and disappear during the iteration process, seriously limiting the progress of the flow simulation in time. By using a separate phase index it is possible to adopt a more robust criterion, where a liquid phase is evolved only when P_{CO_2} exceeds P_{sat,CO_2} by a finite amount, $P_{CO_2} > 1.001 \times P_{sat,CO_2}$, say. Strictly speaking, a state with $P_{CO_2} > P_{sat,CO_2}$ cannot exist in two-phase aqueous-gas conditions, but allowing P_{CO_2} to slightly exceed P_{sat,CO_2} without evolving liquid entails a small inaccuracy in representing the physical properties of CO_2 , with negligible impacts on longer-term simulation results, while greatly improving the efficiency of the simulation. As will be seen below, transitions from a-g to a-l-g conditions occur frequently when simulating upward migration of CO_2 . It is only through introduction of a finite albeit small window for phase change that this process can be efficiently simulated.

3. Two-dimensional Radially Symmetric System

In practical applications of geologic disposal of CO₂, the injection plumes would reach large areal extent, of the order of 100 km² or more for 30 years of CO₂ disposal from a 1,000 MW coal-fired power plant (Pruess et al., 2003). With plumes this large it is to be expected that injected CO₂ would encounter geologic discontinuities such as fracture zones or faults that may provide preferential pathways for upward migration of CO₂ (Streit and Hillis, 2002). Old abandoned wells may also provide leakage risks in many oil and gas provinces. When supercritical CO₂ migrates upward from depth, its thermodynamic state will change towards lower pressures and temperatures, and a transition to sub-critical conditions may take place (Fig. 1.2). Eventually the liquid CO₂ will boil into gas, a process that involves significant heat transfer effects due to the latent heat of vaporization (Fig. 2.3). The thermal effects make the process multi-dimensional even under idealized conditions where upflow would be confined to a vertical 1-D channel with impermeable boundaries. The simplest geometry in which the coupling between fluid flow and heat transfer can be modeled involves a two-dimensional radially symmetric (2-D R-Z) system, in which a permeable channel at the center may exchange heat with the surrounding rock. This is the geometric configuration adopted here for a first exploration of phase change effects during upward migration of CO₂. In investigating this simplified system, our purpose is to bring out the main fluid and thermodynamic effects that determine the behavior of CO₂ discharge from a geologic disposal reservoir. Future work should aim at a more realistic description of potential CO₂ storage reservoirs, and geometric and hydrogeologic properties of potential pathways for CO₂ leaks (Hitchon et al., 1999).

We consider a flow system in the shape of a cylinder with 200 m radius and 1000 m vertical thickness (see Fig. 3.1). A vertical channel of 3 m radius with a high permeability of 10⁻¹³ m² is located at the center, while the surrounding medium is modeled as homogeneous and isotropic with a permeability of 10⁻¹⁴ m², a factor 10 smaller than the channel. Boundary conditions at the land surface include an atmospheric pressure of 1.013 bar and a temperature of 5 °C. (Our model does not include an unsaturated zone so that, strictly speaking, these conditions apply at the elevation of the water table rather than at the land surface.) Prior to introducing CO₂ into the channel, an initial state is prepared that corresponds to a hydrostatic pressure profile and to steady heat flow with a geothermal gradient of 30 °C per km, typical for continental crust. Injection is then initiated by applying CO₂ at the bottom boundary of the channel at a pressure of 100 bar, which is considered a very modest overpressure in comparison to the equilibrated water pressure of 99.07 bar at this elevation. Temperature at the bottom boundary is maintained at 35 °C, and pressure and temperature conditions at the outer (lateral) boundary are maintained constant at their initial values. Other problem parameters are given in Tables 3.1 and 3.2. At the present time no experimental data are

available for constitutive properties (three-phase relative permeabilities and capillary pressures) of brine-CO₂ mixtures. We use Stone's (1970) three-phase water-oil-gas relative permeability formulation, assuming that water will be wetting and gaseous CO₂ non-wetting, with liquid CO₂ having intermediate wettability. Relative permeability parameters were chosen as in a typical three-phase flow problem involving water, soil gas, and a non-aqueous phase liquid (NAPL); more specifically, we use the same parameters as in the benzene-toluene flow problem presented as sample problem # 5 for TMVOC (Pruess and Battistelli, 2002). Capillary pressures were neglected.

For numerical simulation the system is discretized into 50 layers of 20 m thickness each. In the radial direction we use 27 grid blocks, starting with $\Delta R = 1$ m in the center, and using larger ΔR at larger distance from the channel. Results are presented in Figs. 3.2 - 3.12.

The CO₂ entering the column partially dissolves in the aqueous phase, but most of it forms a separate liquid phase. Fig. 3.2 shows snapshots of the CO₂ plume at three different times. The CO₂ migrates primarily upward and also laterally outward from the high-permeability channel, reaching the land surface after 29.1 years. Over time the CO₂ displaces more water, causing an increase in CO₂ mobility and flow rates (Fig. 3.3). CO₂ inventory tracks total amount of CO₂ injected at early time, but grows more slowly at later time because CO₂ discharges at increasing rates at the top (Figs. 3.3-4). CO₂ rises as a liquid phase and flashes into gaseous CO₂ at a depth of approximately 630 m (Figs. 3.5-8), at thermodynamic conditions corresponding to the intersection of the profile of initial temperature and pressure conditions with the saturation line for CO₂ ($T = 23.9$ °C, $P = 62.8$ bar; Fig. 1.2). The vaporization is partial and gives rise to evolution of a three-phase zone. As will be discussed in more detail below, the three-phase zone is a region of diminished fluid mobility which impedes upward migration of CO₂. This enhances lateral flow, causing a broadening of the CO₂ plume, and giving rise to more dispersed CO₂ discharge at the land surface.

The processes of fluid flow, CO₂ dissolution, and phase change are accompanied by significant temperature effects (Figs. 3.9-11). At early time there is a modest temperature increase of approximately 3 °C in the two-phase (aqueous-liquid) zone, due to heat of dissolution of CO₂. After a three-phase zone has formed, temperatures decline in the region of most intense CO₂ vaporization, near the top of the three-phase zone. The temperature decline from boiling of liquid CO₂ causes conductive cooling near the front. As the liquid front advances upward (Fig. 3.5) the three-phase zone becomes very broad (Figs. 3.7-8). Large gradients in phase saturations occur at the bottom and at the top boundary of the three-phase zone. Our simulation stops after 391.2 years

as freezing conditions are approached, because the fluid property treatment adopted here has no provisions to deal with phase change from liquid water to ice or solid hydrate phases.

Fig. 3.11 shows that the upward advancement of the liquid front slows down with time, while frontal temperatures become lower and always remain close to CO₂ saturation temperature at prevailing pressure. This behavior can be understood from the linkage between pressures and temperatures in three-phase conditions (two-phase liquid-gas conditions for CO₂). Fluid pressures never deviate much from the original hydrostatic values (Fig. 3.12), and partial pressure of water vapor is small at the temperatures considered here. Wherever free-phase CO₂ is present, its partial pressure is always approximately equal to the initial hydrostatic pressure at the same elevation. When liquid CO₂ enters a region where gaseous CO₂ is present, vaporization will be complete as long as the prevailing temperature remains above the saturation line, $T > T_{\text{sat}}(P_{\text{CO}_2})$. The vaporization process lowers temperatures and eventually gives rise to evolution of a liquid phase when the temperature drops to the saturated vapor temperature of CO₂ at prevailing pressure. Fig. 3.10b shows that the (T, P) profile tracks the CO₂ saturation line throughout the three-phase zone. Because the pressure of gaseous CO₂ is always close to hydrostatic pressure, and therefore is smaller at shallower depths, increasingly prolonged boiling is required to induce the larger temperature drops needed for advancement of the liquid CO₂ front. This explains why the advancement of the liquid front slows down over time. We can conclude that the advancement of the liquid front is entirely dominated by the thermal aspects of the problem.

Fluid mobilities are reduced in the three-phase zone from interference between the phases. This reduces flow rates in the vertical direction, slows the advancement of the liquid front (Fig. 3.11), and gives rise to lateral plume broadening and more dispersed discharge at the land surface (Fig. 3.4). Gas saturations increase to very large values due to decompression effects as the CO₂ approaches the land surface (Figs. 3.6-7).

4. Forced-isothermal Conditions

In order to bring out more clearly the specific flow effects caused by heat transfer, a comparison case was run in which a very large heat capacity was specified for the rock, so that temperatures remain unchanged at the initial geothermal gradient. In this case both temperatures and pressures increase monotonically with depth, so that along any vertical line there will be only one point at which the CO₂ saturation line is intersected. At this point a sharp transition from two-phase aqueous-liquid conditions below to aqueous-gas conditions above will take place, so that no formation of a three-phase zone is expected. This is confirmed by our simulation.

In Fig. 4.1, the region with two-phase aqueous-liquid conditions extends upward to about 610 m depth, and is overlain by a two-phase region with aqueous-gas conditions. Absence of a three-phase zone means that there is no region of severely reduced fluid mobility as had been encountered in the non-isothermal simulation. Accordingly, there is less resistance to upflow of CO₂, especially near the center where phase interference had been most severe in the non-isothermal case. As a consequence, there is less lateral plume broadening. CO₂ fluxes at the land surface show a more pronounced and more persistent maximum near $R = 0$, and drop off more rapidly with increasing R than in the non-isothermal case (Fig. 4.2). At late time, CO₂ fluxes at large radius are actually larger for the non-isothermal case. Fig. 4.3 shows cumulative CO₂ discharge rates at the land surface out to a distance R from the high- k channel as a function of R . Total discharges of CO₂ are seen to be smaller in the non-isothermal case, reflecting the mobility blockage in the three-phase zone.

CO₂ inflow rates at the bottom and total injected CO₂ mass are virtually identical in both cases, which is remarkable given the rather different flow behavior and patterns of liquid and gas saturations in the two cases. The larger outflow at the land surface in the forced-isothermal case implies that CO₂ inventory in the flow system should be smaller for forced-isothermal conditions, which is borne out by a tabulation of mass balances (Table 4.1). In the non-isothermal case, growth of CO₂ inventory with time is due to both liquid CO₂ and CO₂ dissolved in the aqueous phase. In the forced-isothermal case, liquid phase and total CO₂ inventories actually decline somewhat from 143.6 to 391.2 yr.

5. Larger Temperature at Top Boundary

It is of interest to investigate whether strong cooling effects can also occur when the initial temperature and pressure profile does not intersect the CO₂ saturation line. Accordingly, another simulation was performed for the case with $T_{ls} = 15$ °C in which CO₂ migrating upward can pass from supercritical to gaseous conditions without a phase change (Fig. 1.2). Results for the evolution of temperature and pressure conditions in the central upflow channel are shown in Fig. 5.1. It is seen that in the region with supercritical pressures, temperatures rapidly decline towards a line that is an extension of the CO₂ saturation line, where enthalpy increases upon CO₂ decompression are largest (Fig. 2.4). The cooling effects push the flow system towards the critical point, and subsequent evolution proceeds along the liquid-gas phase boundary, similar to what was seen in the $T_{ls} = 5$ °C case. The simulation was terminated after 1,214 years, at which time a minimum temperature of 8.3 °C had been reached at 430 m depth.

6. Concluding Remarks

Supercritical CO₂ escaping from a deep disposal reservoir may migrate along sub-vertical preferential pathways, such as fracture zones and faults, or old abandoned wells, and may eventually discharge at the land surface. CO₂ migration is affected by permeability structure and multiphase fluid and heat transfer effects that include liquid CO₂ boiling into gas. This consumes large amounts of latent heat and causes considerable cooling of the rock. A three-phase fluid zone (aqueous - liquid CO₂ - gaseous CO₂) may form which may become very thick as the liquid CO₂ front advances upward. The test case studied here involved a very modest leakage rate of approximately 0.3 kg/s, which corresponds to less than 0.1 % of the rate at which CO₂ would be generated from a 1,000 MW coal-fired power plant (Hitchon, 1996). The three-phase zone in our simulation grew to over 200 m in thickness after 391.2 years of CO₂ discharge. Fluid mobility is reduced in the three-phase zone from interference between the phases. This reduces rates of CO₂ upflow, causes the CO₂ plume to broaden laterally, and gives rise to smaller and more dispersed CO₂ discharges at the land surface than would be observed if no three-phase zone developed.

Maximum boiling rates and strongest temperature declines occur near the top of the three-phase zone. A simulation for an average land surface temperature of $T_{ls} = 5\text{ }^{\circ}\text{C}$ was terminated after 391.2 years, when minimum temperatures had declined to below $3\text{ }^{\circ}\text{C}$. At this point, the liquid CO₂ had advanced to a depth of 350 m. A simulation for $T_{ls} = 15\text{ }^{\circ}\text{C}$ reached a minimum temperature of $8.3\text{ }^{\circ}\text{C}$ at 430 m depth after 1,214 years. The results presented here suggest that temperatures would eventually drop below the freezing point of water if the flow process were run out longer. Solid water ice and hydrate phases would then form and reduce the permeability of the preferential CO₂ pathway, reducing gas fluxes and dispersing discharges at the land surface over a larger area. The fluid property module developed here has no provisions at present for representing solid phases other than salt.

In realistic groundwater systems another effect would come into play that could substantially reduce upflow of CO₂. Regional groundwater flow may dissolve and remove significant amounts of CO₂, reducing rates of upward migration of free-phase CO₂. This effect requires a fully 3-D analysis and could not be represented in our axisymmetric model. Future work should also aim at a more realistic representation of geometric and hydrogeologic properties of potential pathways for CO₂ migration towards shallower strata, including features such as anisotropic, layered formations, and additional flow barriers such as shale layers that may divert CO₂ upflow sideways until another zone of caprock weakness is encountered. Model predictions are sensitive to constitutive properties for three-phase flows of water and liquid-gas mixtures of CO₂ for which no experimental results are available at present.

Acknowledgement

The author is grateful to Curt Oldenburg and George Moridis for their incisive reviews and helpful suggestions. This work was supported by the Director, Office of Science, Office of Basic Energy Sciences of the U.S. Department of Energy under Contract No. DE-AC03-76SF00098.

References

- Adenekan, A.E., T.W. Patzek and K. Pruess. Modeling of Multiphase Transport of Multicomponent Organic Contaminants and Heat in the Subsurface: Numerical Model Formulation, *Water Resour. Res.*, Vol. 29, No. 11, pp. 3727-3740, 1993.
- Altunin, V.V. *Thermophysical Properties of Carbon Dioxide*, Publishing House of Standards, 551 pp., Moscow, 1975 (in Russian).
- Battistelli, A., C. Calore and K. Pruess. The Simulator TOUGH2/EWASG for Modeling Geothermal Reservoirs with Brines and Non-Condensable Gas, *Geothermics*, Vol. 26, No. 4, pp. 437 - 464, 1997.
- Chivas, A.R., I. Barnes, W.C. Evans, J.E. Lupton and J.O. Stone. Liquid Carbon Dioxide of Magmatic Origin and its Role in Volcanic Eruptions, *Nature*, Vol. 326, No. 6113, pp. 587 - 589, 9 April 1987.
- DOE. *Carbon Sequestration Research and Development*, D. Reichle et al. (eds.), U.S. Department of Energy Report DOE/SC/FE-1, Washington, DC, 1999.
- Hitchon, B. (ed.). *Aquifer Disposal of Carbon Dioxide*, Geoscience Publishing, Ltd., Sherwood Park, Alberta, Canada, 1996.
- Hitchon, B., W.D. Gunter, T. Gentzis and R.T. Bailey. Sedimentary Basins and Greenhouse Gases: A Serendipitous Association, *Energy Convers. Mgmt.*, Vol. 40, pp. 825 - 843, 1999.
- Holloway, S. An Overview of the Underground Disposal of Carbon Dioxide, *Energy Convers. Mgmt.*, Vol. 38, Suppl., pp. S193 - S198, 1997.
- Holloway, S. and D. Savage. The Potential for Aquifer Disposal of Carbon Dioxide in the U.K., *Energy Convers. Mgmt.*, Vol. 34, No. 9 - 11, pp. 925 - 932, 1993.
- International Formulation Committee. *A Formulation of the Thermodynamic Properties of Ordinary Water Substance*, IFC Secretariat, Düsseldorf, Germany, 1967.
- IPCC (Intergovernmental Panel on Climate Change). *Climate Change 1995: The Science of Climate Change*, J.T. Houghton et al. (eds.), Cambridge University Press, Cambridge, United Kingdom, 1996.
- Keeling, C.D. and T.P. Whorf. Atmospheric CO₂ Records from Sites in the SIO Air Sampling Network, in: *Trends: A Compendium of Data on Global Change*, Carbon Dioxide Information Analysis Center, Oak Ridge National Laboratory, Oak Ridge, TN, 1998.
- Kongsjorden, H., O. Karstad and T.A. Torp. Saline Aquifer Storage of Carbon Dioxide in the Sleipner Project, *Waste Management*, Vol. 17, No. 5/6, pp. 303 - 308, 1997.

- Korbøl, R. and A. Kaddour. Sleipner Vest CO₂ Disposal - Injection of Removed CO₂ into the Utsira Formation, *Energy Convers. Mgmt.*, Vol. 36, No. 6 - 9, pp. 509 - 512, 1995.
- Ledley, T.S., E.T. Sundquist, S.E. Schwartz, D.K. Hall, J.D. Fellows, and T.L. Killeen. Climate Change and Greenhouse Gases, *EOS*, Transactions Am. Geoph. Union, Vol. 80, No. 39, pp. 453 - 458, 1999.
- Lindeberg, E., P. Zweigel, P. Bergmo, A. Ghaderi, and A. Lothe. Prediction of CO₂ Distribution Pattern Improved by Geologic and Reservoir Simulation and Verified by Time Lapse Seismic, in: D. Williams et al. (eds.), *Proceedings, Fifth International Conference on Greenhouse Gas Control Technologies*, pp. 372 - 377, CSIRO Publ., Collingwood, VIC, Australia, 2001.
- Moridis, G. and K. Pruess. T2SOLV: An Enhanced Package of Solvers for the TOUGH2 Family of Reservoir Simulation Codes, *Geothermics*, Vol. 27, No. 4, pp. 415 - 444, 1998.
- O'Sullivan, M.J., G.S. Bodvarsson, K. Pruess and M.R. Blakeley. Fluid and Heat Flow in Gas-rich Geothermal Reservoirs, *Soc. Pet. Eng. J.*, 25 (2), 215-226, 1985.
- Pruess, K., C. Oldenburg and G. Moridis. *TOUGH2 User's Guide, Version 2.0*, Lawrence Berkeley National Laboratory Report LBNL-43134, Berkeley, CA, November 1999.
- Pruess, K. and A. Battistelli. *TMVOC, a Numerical Simulator for Three-Phase Non-Isothermal Flows of Multicomponent Hydrocarbon Mixtures in Saturated-Unsaturated Heterogeneous Media*, Lawrence Berkeley National Laboratory Report LBNL-49375, Berkeley, CA, April 2002.
- Pruess, K. and J. García. Multiphase Flow Dynamics During CO₂ Injection into Saline Aquifers, *Environmental Geology*, Vol. 42, pp. 282 - 295, 2002.
- Pruess, K., T. Xu, J. Apps and J. García. Numerical Modeling of Aquifer Disposal of CO₂, Paper SPE-83695, *SPE Journal*, pp. 49 - 60, 2003.
- Sigurdsson, H., J.D. Devine, F.M. Tchoua, T.S. Presser, M.K.W. Pringle, and W.C. Evans. Origin of the Lethal Gas Burst from Lake Monoun, Cameroon, *J. Volcanol. Geotherm. Res.*, Vol. 31, pp. 1 - 16, 1987.
- Stone, H.L. Probability Model for Estimating Three-Phase Relative Permeability, *Trans. SPE of AIME*, 249, 214-218, 1970.
- Streit, J.E. and R.R. Hillis. Building Geomechanical Models for the Safe Underground Storage of Carbon Dioxide in Porous Rock, paper H1-1, presented at Sixth International Conference on Greenhouse Gas Technologies (GHGT-6), Kyoto, Japan, October 1-4, 2002.
- Tazieff, H. Mechanism of the Nyos Carbon Dioxide Disaster and of so-called Phreatic Steam Eruptions, *J. Volcanol. Geotherm. Res.*, Vol. 391, pp. 109 - 116, 1991.
- Torp, T.A. and J. Gale. Demonstrating Storage of CO₂ in Geologic Reservoirs: The Sleipner and SACS Projects, paper B1-1, presented at Sixth International Conference on Greenhouse Gas Technologies (GHGT-6), Kyoto, Japan, October 1-4, 2002.
- Vargaftik, N.B. *Tables on the Thermophysical Properties of Liquids and Gases*, 2nd Ed., John Wiley & Sons, New York, NY, 1975.

Zweigel, P. and J. Gale. Storing CO₂ Underground Shows Promising Results, *EOS Trans.*, Vol. 81, No. 45, November 7, 2000.

Tables

Table 2.1. Primary thermodynamic variables used for multiphase mixtures of water, CO₂, and salt.
(P - pressure, X - CO₂ mass fraction, S - saturation, T - temperature; X_{sm} is dissolved salt mass fraction or pore volume fraction of precipitated salt)

Phase Conditions	Abbreviation	Phase Index	Primary Variables			
			X1	X2	X3	X4
aqueous only	a	1	P	X _{sm}	X	T
liquid only	l	2	P	X _{sm}	X	T
gas only	g	3	P	X _{sm}	X	T
aqueous and liquid	a-l	4	P	X _{sm}	S _a	T
aqueous and gas	a-g	5	P	X _{sm}	S _a	T
liquid and gas	l-g	6	P	X _{sm}	S _g	T
three phase	a-l-g	7	P	X _{sm}	S _a	S _g

Table 3.1. Hydrogeologic parameters for 2-D R-Z model of CO₂ leak.

Permeability	
channel	$k = 10^{-13} \text{ m}^2$
surrounding rock	$k = 10^{-14} \text{ m}^2$
Porosity	$\phi = 0.35$
Pore compressibility	$c = 4.5 \times 10^{-10} \text{ Pa}^{-1}$
Relative permeability: Stone's first 3-phase method (Stone, 1970)	
a - aqueous phase	
$k_{ra} = \left[\frac{S_a - S_{ar}}{1 - S_{ar}} \right]^n$	
irreducible aqueous phase saturation	$S_{ar} = 0.15$
exponent	$n = 3$
l - liquid phase	
$k_{rl} = \left[\frac{\hat{S} - S_a}{\hat{S} - S_{ar}} \right] \left[\frac{1 - S_{ar} - S_{lr}}{1 - S_a - S_{lr}} \right]$	$\hat{S} = 1 - S_g - S_{lr}$
$* \left[\frac{(\hat{S} - S_{ar})(1 - S_a)}{(1 - S_{ar})} \right]^n$	
irreducible liquid phase saturation	$S_{lr} = 0.05$
exponent	$n = 3$
g - gas phase	
$k_{rg} = \left[\frac{S_g - S_{gr}}{1 - S_{ar}} \right]^n$	
irreducible gas phase saturation	$S_{gr} = 0.01$
exponent	$n = 3$
Capillary pressure	$P_{cgl} = 0$ $P_{cga} = 0$
Thermal parameters	
thermal conductivity	$2.51 \text{ W/m } ^\circ\text{C}$
specific heat	$920 \text{ J/kg } ^\circ\text{C}$
rock grain density	2600 kg/m^3

Table 3.2. Initial conditions and injection specifications

Temperature	5 °C at land surface 30 °C/km geothermal gradient
Pressure	1.013 bar at land surface hydrostatic gradient
CO ₂ pressure	100 bar at 1000 m depth
Salinity	0

Table 4.1. CO₂ inventory at different times. The data are for the non-isothermal and isothermal case, respectively.

time (yr)	CO _{2,aq} (tonnes) non-isoth. isoth.	CO _{2,liq} (tonnes) non-isoth. isoth.	CO _{2,gas} (tonnes) non-isoth. isoth.	CO _{2,tot} (tonnes) non-isoth. isoth.
32.0820	36,628.7 36,173.6	155,237.5 151,562.2	1,009.5 729.9	192,875.7 188,465.7
143.640	384,121.1 384,714.1	559,224.5 501,035.0	93,438.6 75,929.7	1,036,784.2 961,678.8
391.221	704,079.1 451,686.6	881,492.7 413,995.7	103,952.2 87,895.5	1,689,524.0 953,577.7

Figure Captions

Figure 1.1. Phase states of CO₂.

Figure 1.2. CO₂ saturation line and hydrostatic pressure-temperature profiles for a typical geothermal gradient of 30 °C/km and two different average temperatures at the land surface.

Figure 1.3. CO₂ density versus depth along the two hydrostatic profiles shown in Fig. 1.2.

Figure 2.1. Possible phase combinations in the system water-CO₂. The phase designations are a - aqueous, l - liquid CO₂, g - gaseous CO₂.

Figure 2.2. Schematic of the temperature-pressure tabulation of CO₂ properties. The saturation line (dashed) is given by the diagonals of interpolation rectangles.

Figure 2.3. Specific enthalpy of gaseous and liquid CO₂ along the saturation line.

Figure 2.4. Specific enthalpy of CO₂ for a range of temperature and pressure conditions.

Figure 3.1. 2-D R-Z flow system.

Figure 3.2. Snapshots of the CO₂ plume at three different times.

Figure 3.3. CO₂ injection rate and mass balance.

Figure 3.4. Profiles of CO₂ flux at the land surface at three different times.

Figure 3.5. Advancement of the liquid CO₂ front in the center of the channel.

Figure 3.6. Profiles of gas saturations vs. time in the center of the channel.

Figure 3.7. Evolution of liquid and gas saturation profiles in the center of the channel (a - 32.08 yr, b - 143.6 yr, c - 391.2 yr).

Figure 3.8. Extent of three-phase zone at three different times. The quantity plotted is the geometric mean of liquid and gas saturations, $S_{liq-gas} = \sqrt{S_{liq} \cdot S_{gas}}$.

Figure 3.9. Temperature distributions (°C) at three different times.

Figure 3.10. Temperature profiles in the center of the upflow channel at different times.

Figure 3.11. Advancement of liquid front, and frontal temperature, as function of time. CO₂ saturation temperatures corresponding to initial hydrostatic pressures at the front are shown as circles.

Figure 3.12. Pressure change relative to the initial hydrostatic profile in the center of the channel.

Figure 4.1. Snapshots of the CO₂ plume in the forced-isothermal case at three different times.

Figure 4.2. Profiles of CO₂ fluxes at the land surface at three different times.

Figure 4.3. Cumulative CO₂ discharge rate, integrated from $R = 0$ outward, at two different times.

Figure 5.1. Temperature-pressure profiles in the central upflow channel for a case with land surface temperature of 15 °C at different times.

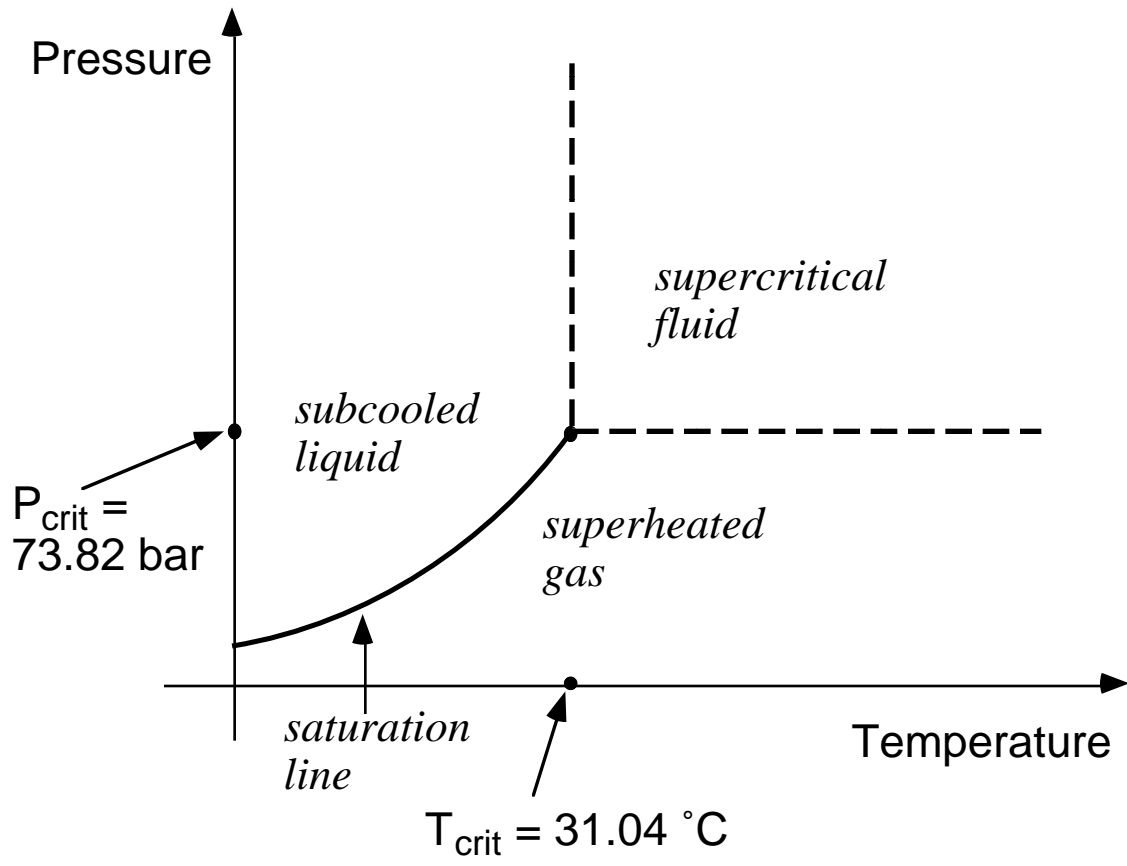


Figure 1.1. Phase states of CO₂.

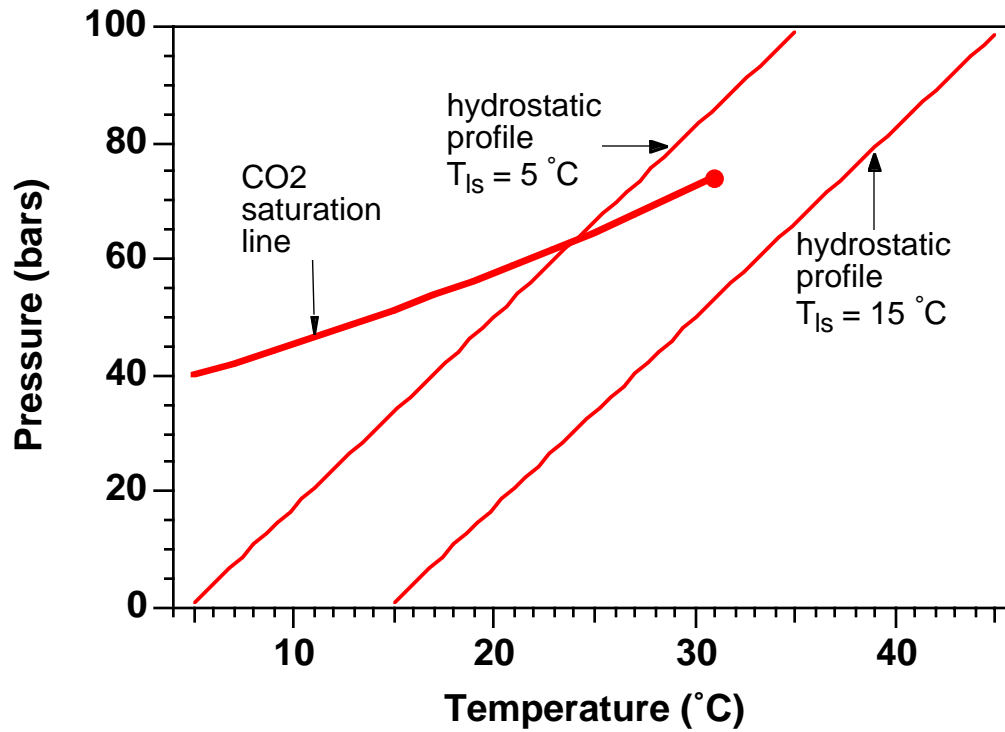


Figure 1.2. CO₂ saturation line and hydrostatic pressure-temperature profiles for a typical geothermal gradient of 30 °C/km and two different average temperatures at the land surface.

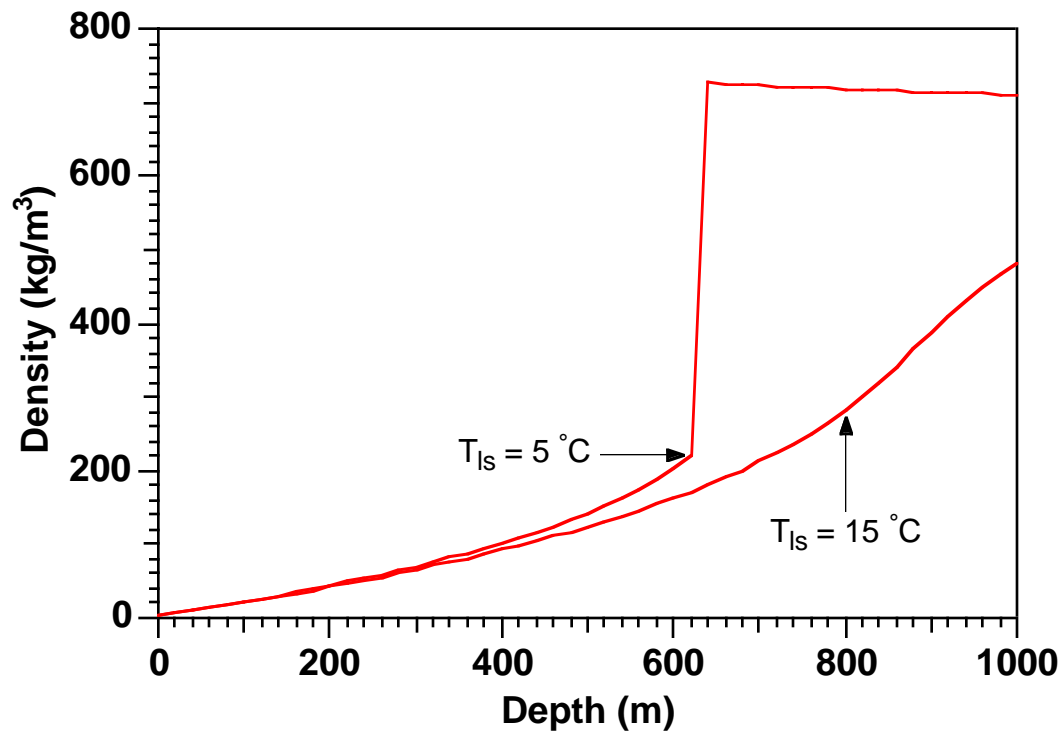


Figure 1.3. CO₂ density versus depth along the two hydrostatic profiles shown in Fig. 1.2.

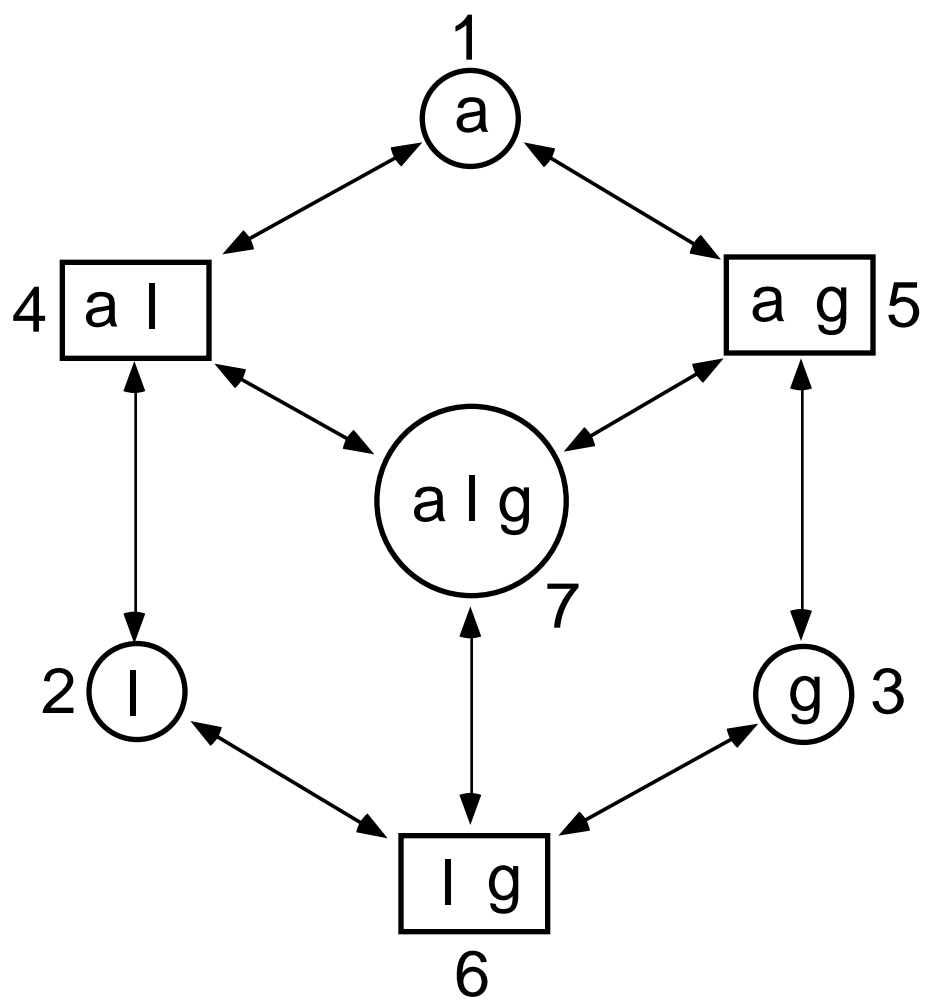


Figure 2.1. Possible phase combinations in the system water-CO₂. The phase designations are a - aqueous, l - liquid CO₂, g - gaseous CO₂.

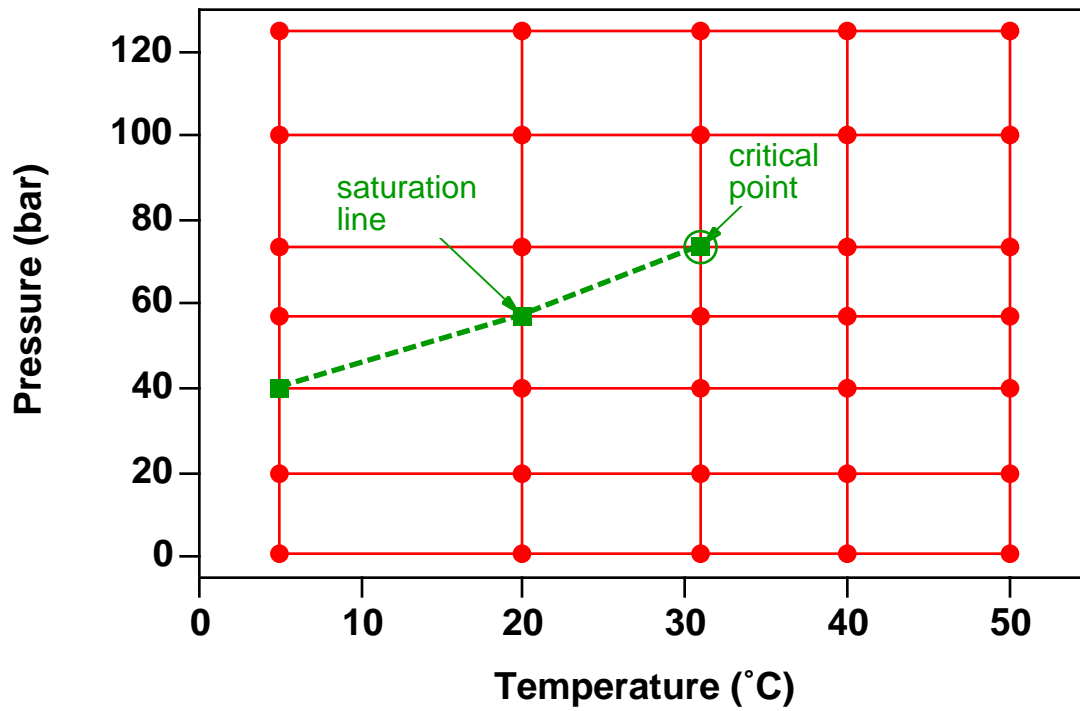


Figure 2.2. Schematic of the temperature-pressure tabulation of CO₂ properties. The saturation line (dashed) is given by the diagonals of interpolation rectangles.

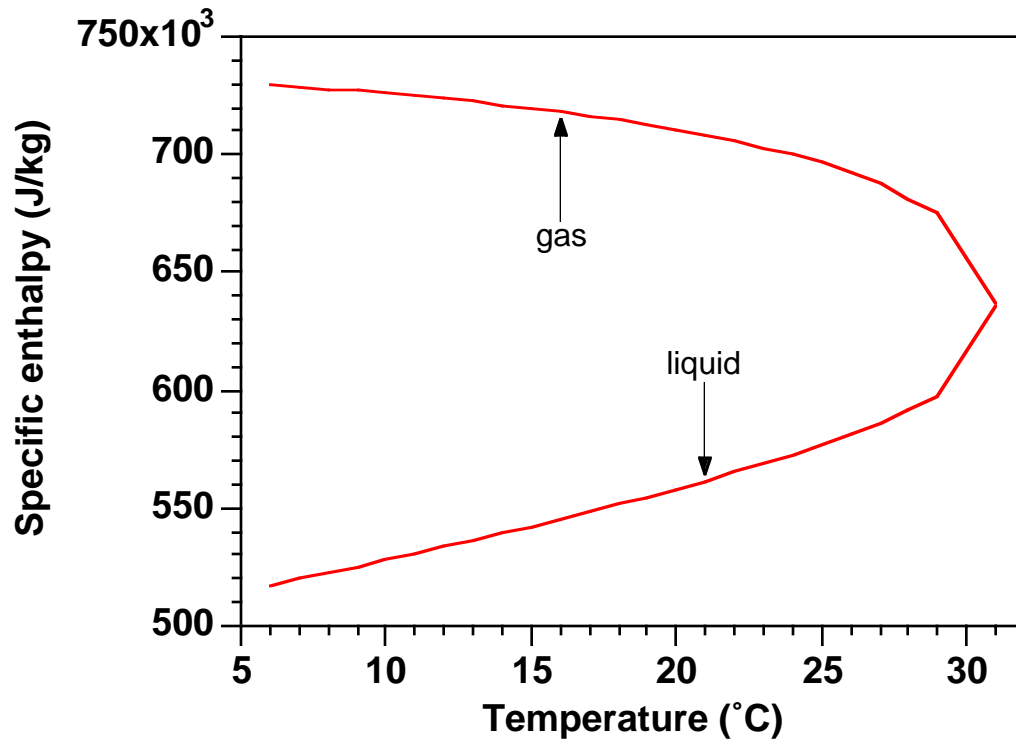


Figure 2.3. Specific enthalpy of gaseous and liquid CO₂ along the saturation line.

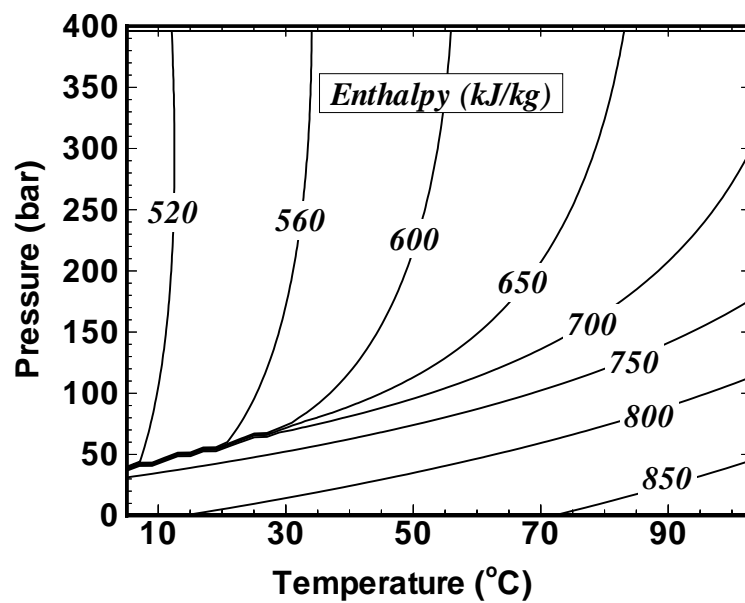


Figure 2.4. Specific enthalpy of CO₂ for a range of temperature and pressure conditions.

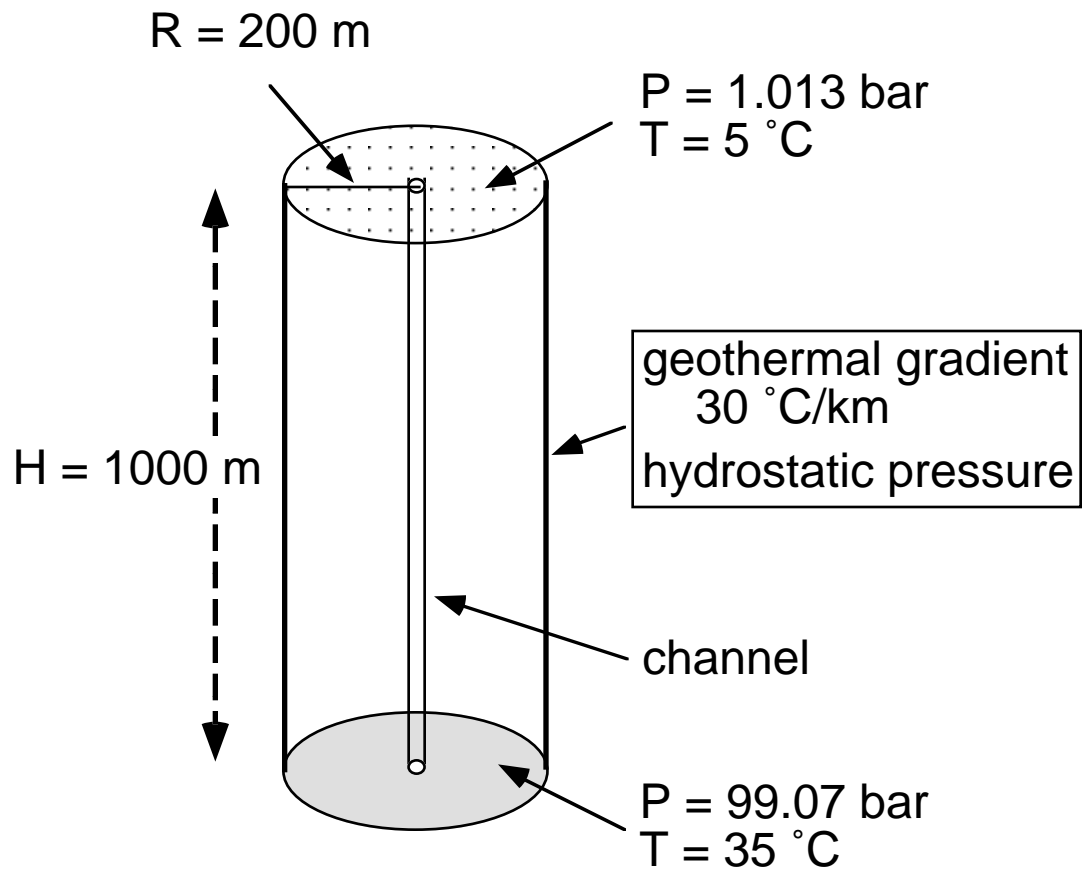


Figure 3.1. 2-D R-Z flow system.

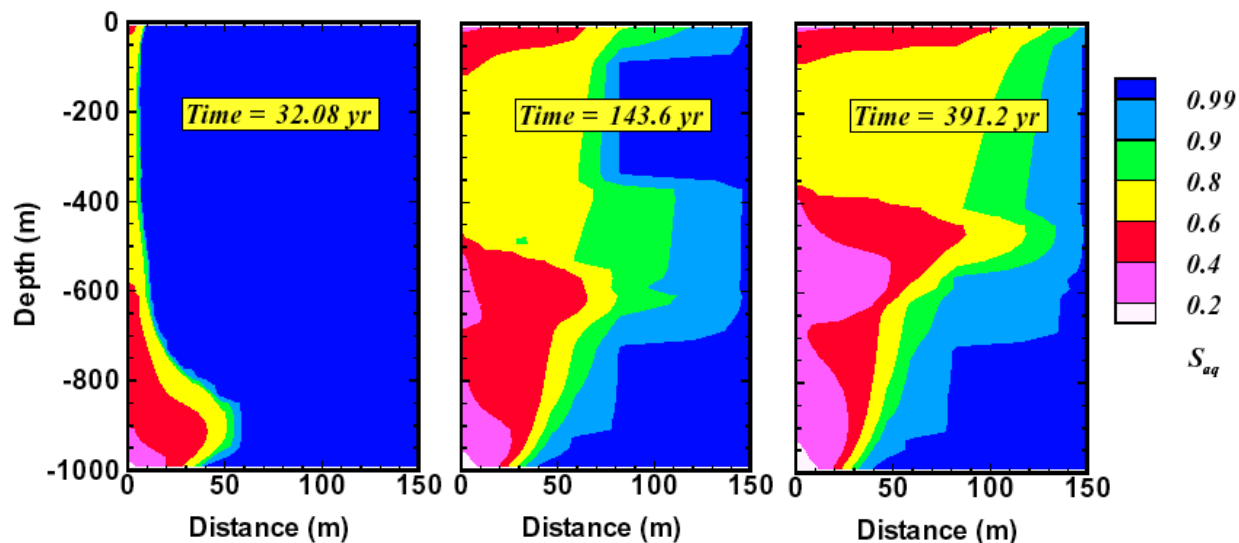


Figure 3.2. Snapshots of the CO₂ plume at three different times.

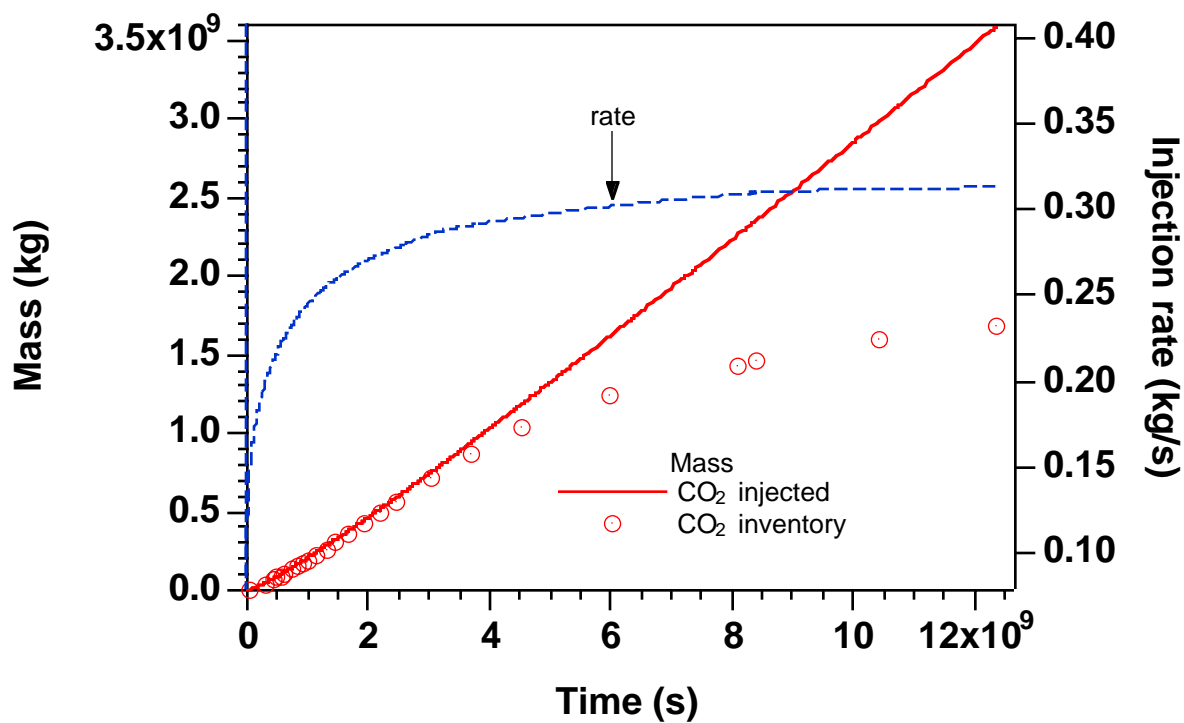


Figure 3.3. CO₂ injection rate and mass balance.

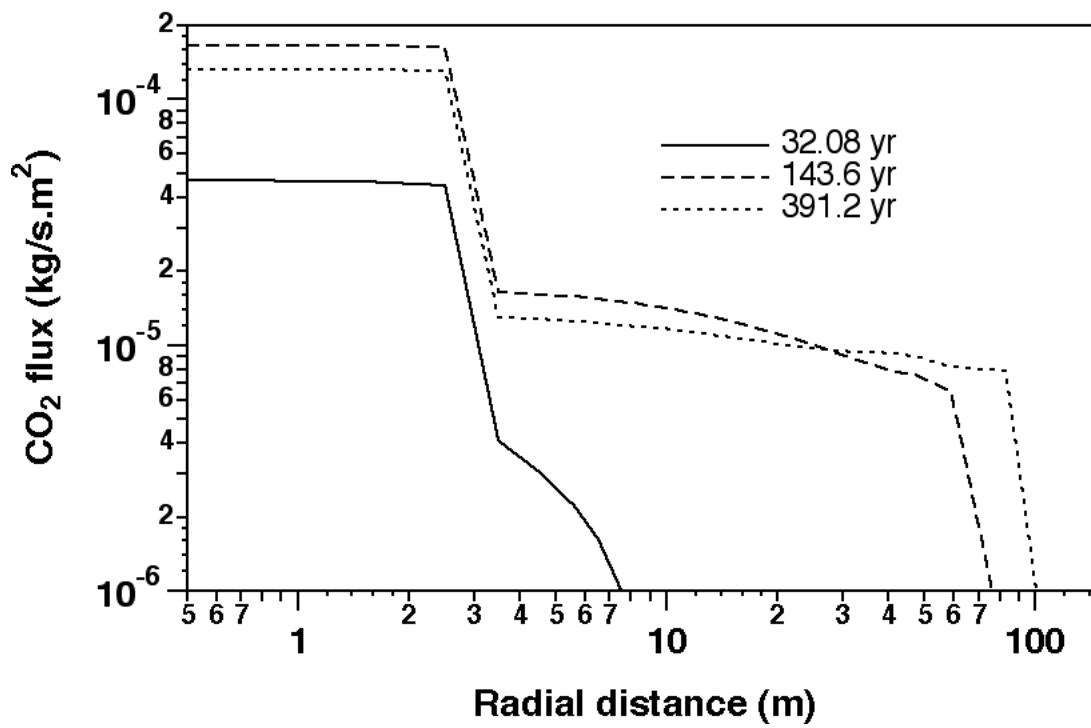


Figure 3.4. Profiles of CO₂ flux at the land surface at three different times.

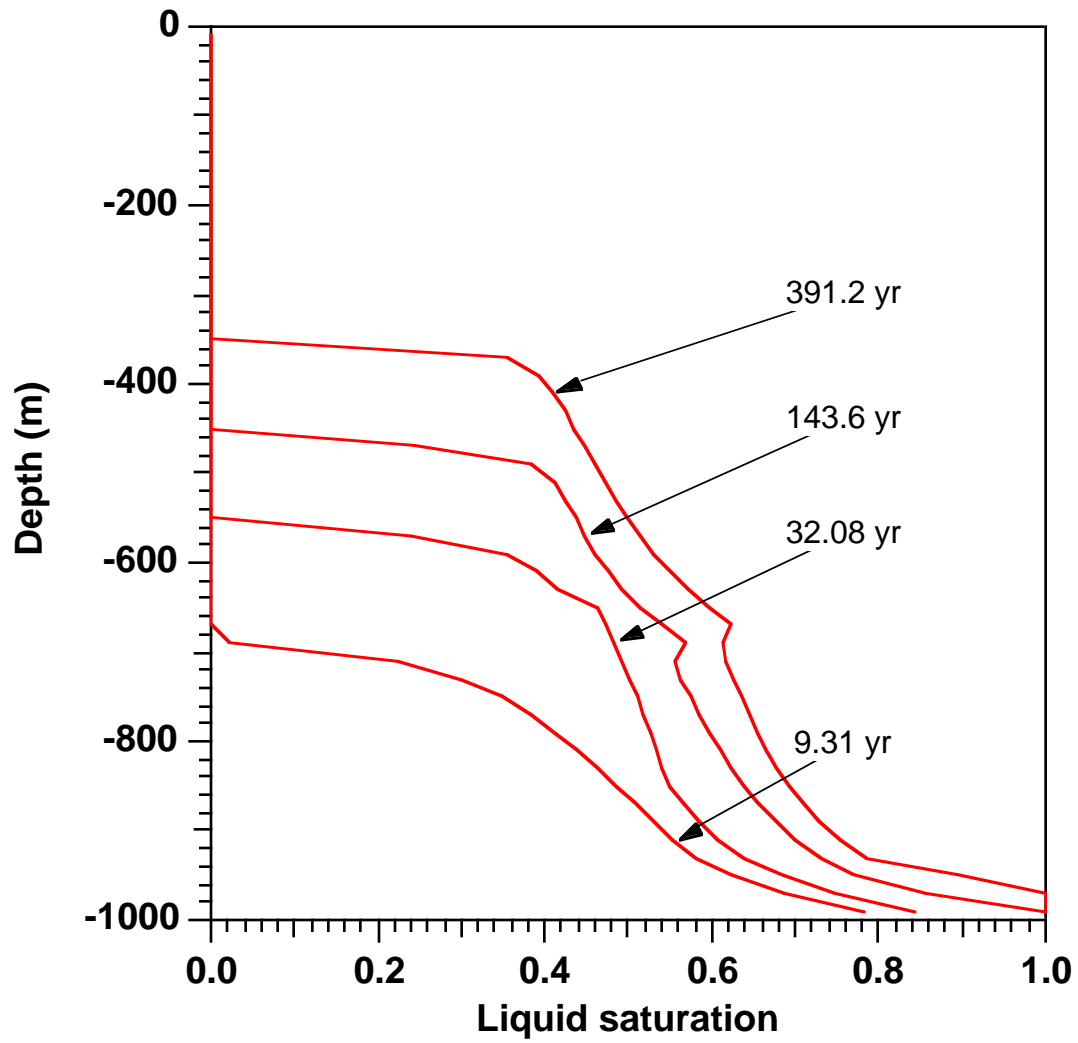


Figure 3.5. Advancement of the liquid CO₂ front in the center of the channel.

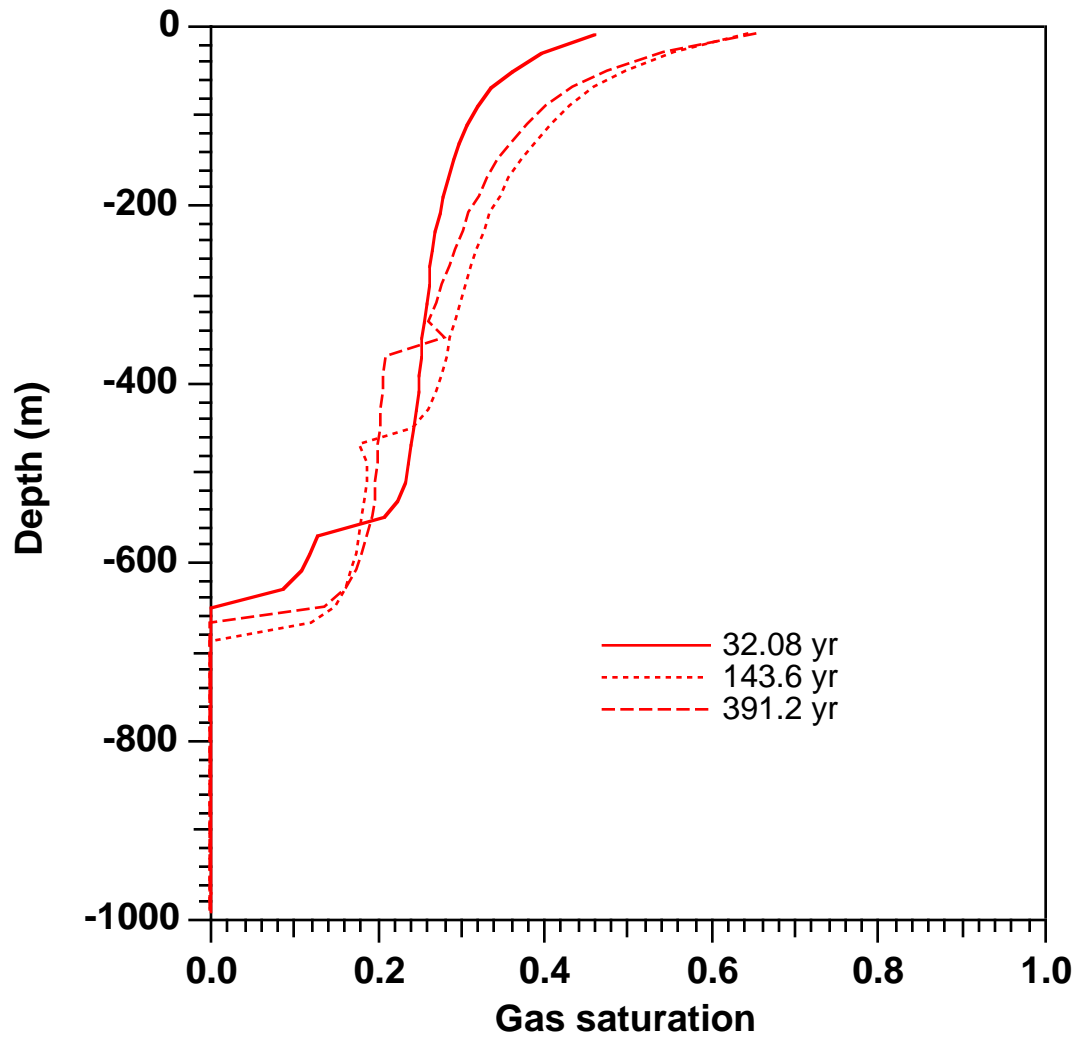


Figure 3.6. Profiles of gas saturations vs. time in the center of the channel.

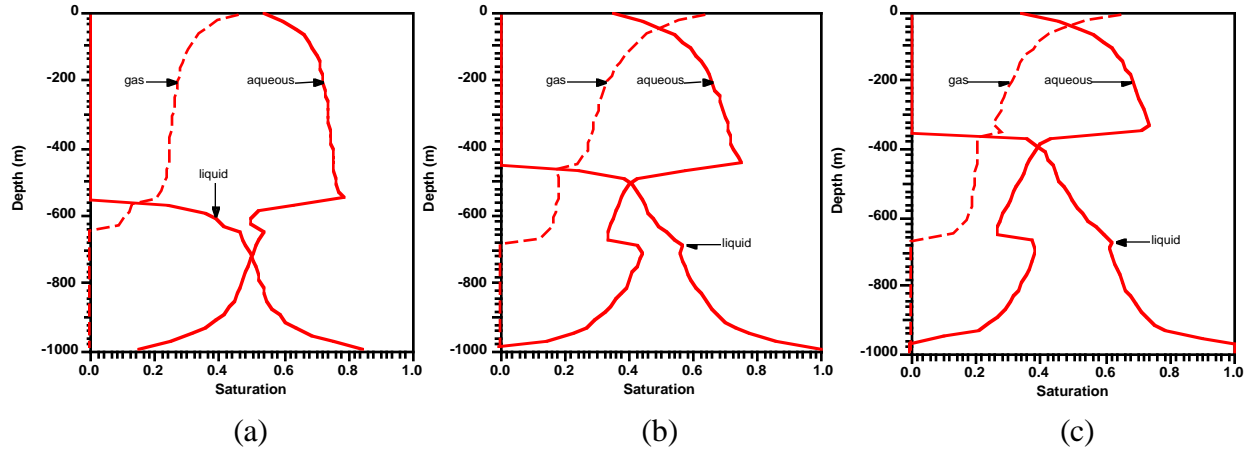


Figure 3.7. Evolution of liquid and gas saturation profiles in the center of the channel
(a - 32.08 yr, b - 143.6 yr, c - 391.2 yr).

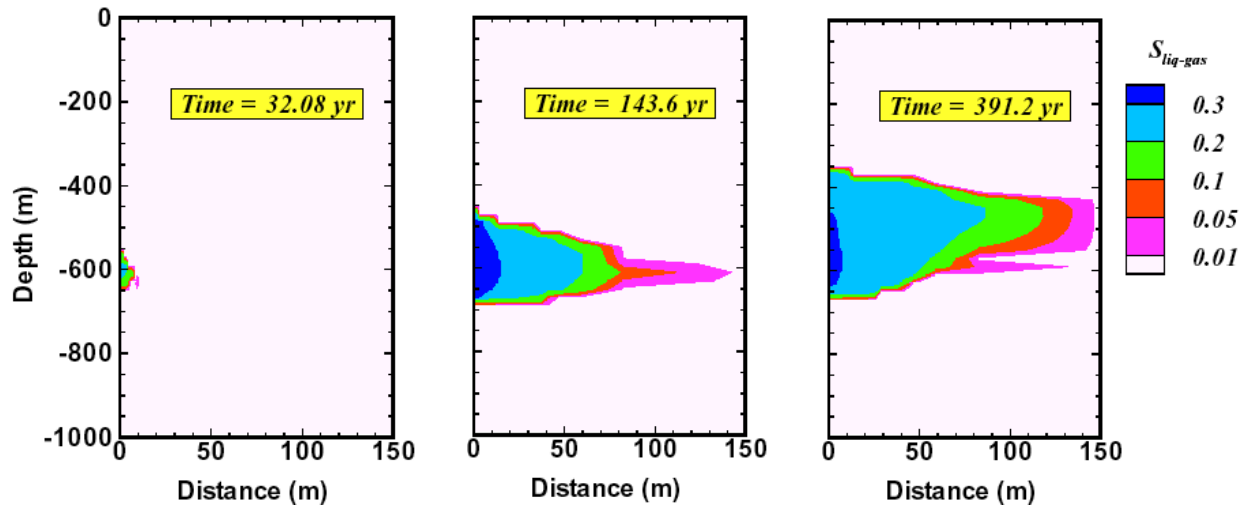


Figure 3.8. Extent of three-phase zone at three different times. The quantity plotted is the geometric mean of liquid and gas saturations, $S_{liq-gas} = \sqrt{S_{liq} \cdot S_{gas}}$.

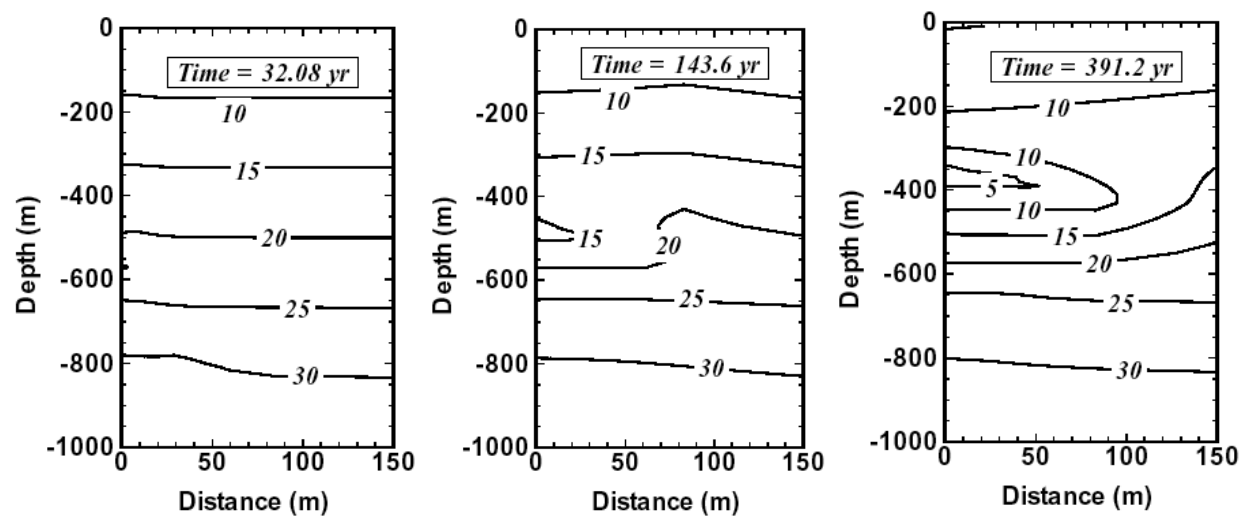
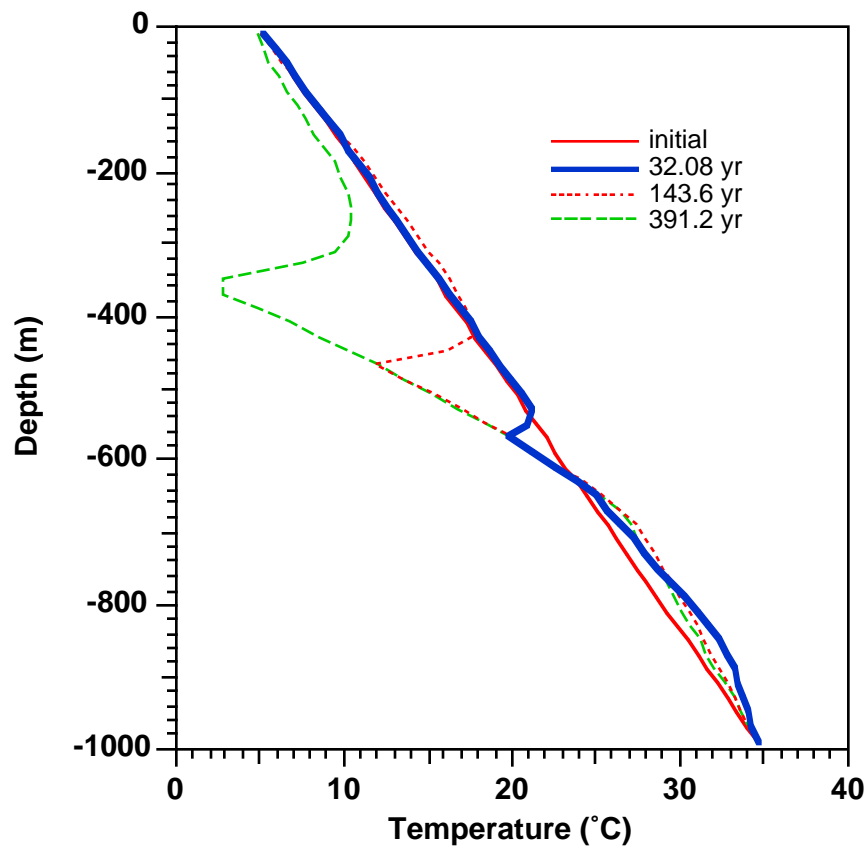
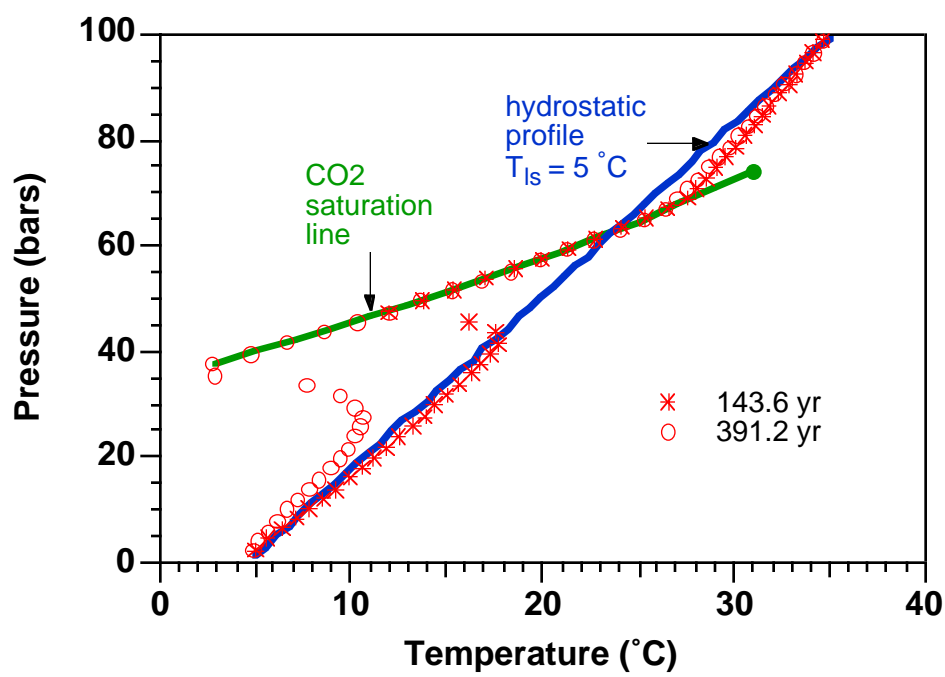


Figure 3.9. Temperature distributions ($^{\circ}\text{C}$) at three different times.



(a)



(b)

Figure 3.10. Temperature profiles in the center of the upflow channel at different times.

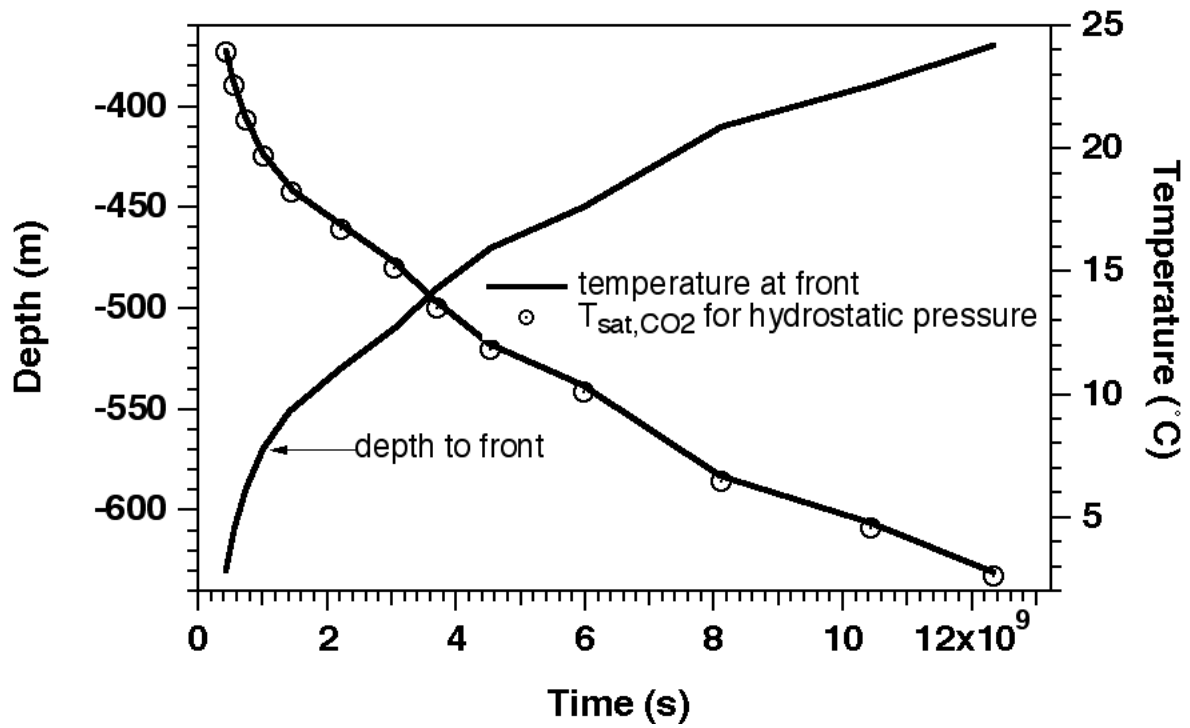


Figure 3.11. Advancement of liquid front, and frontal temperature, as function of time. CO₂ saturation temperatures corresponding to initial hydrostatic pressures at the front are shown as circles.

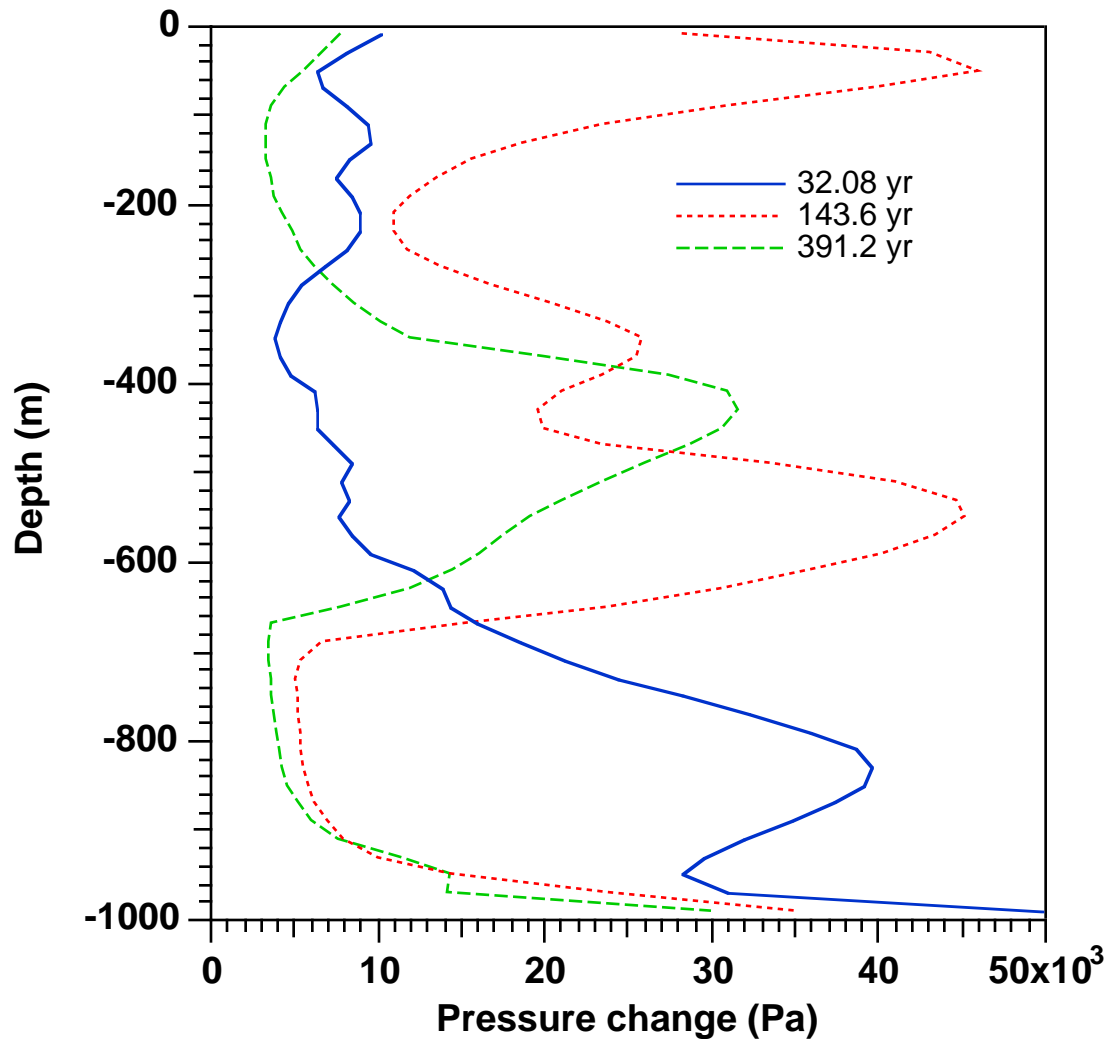


Figure 3.12. Pressure change relative to the initial hydrostatic profile in the center of the channel.

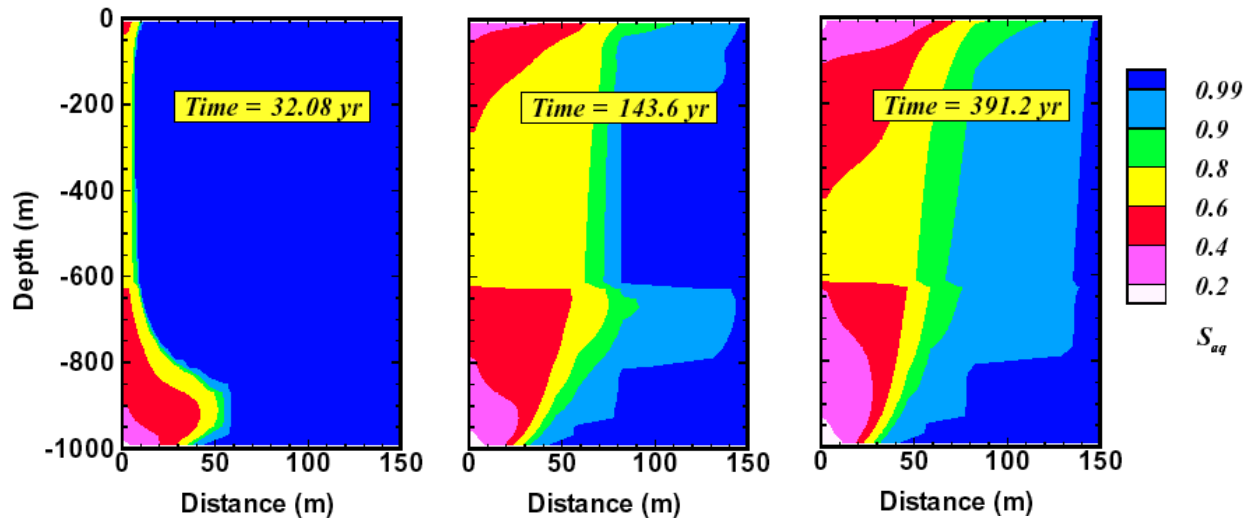


Figure 4.1. Snapshots of the CO₂ plume in the forced-isothermal case at three different times.

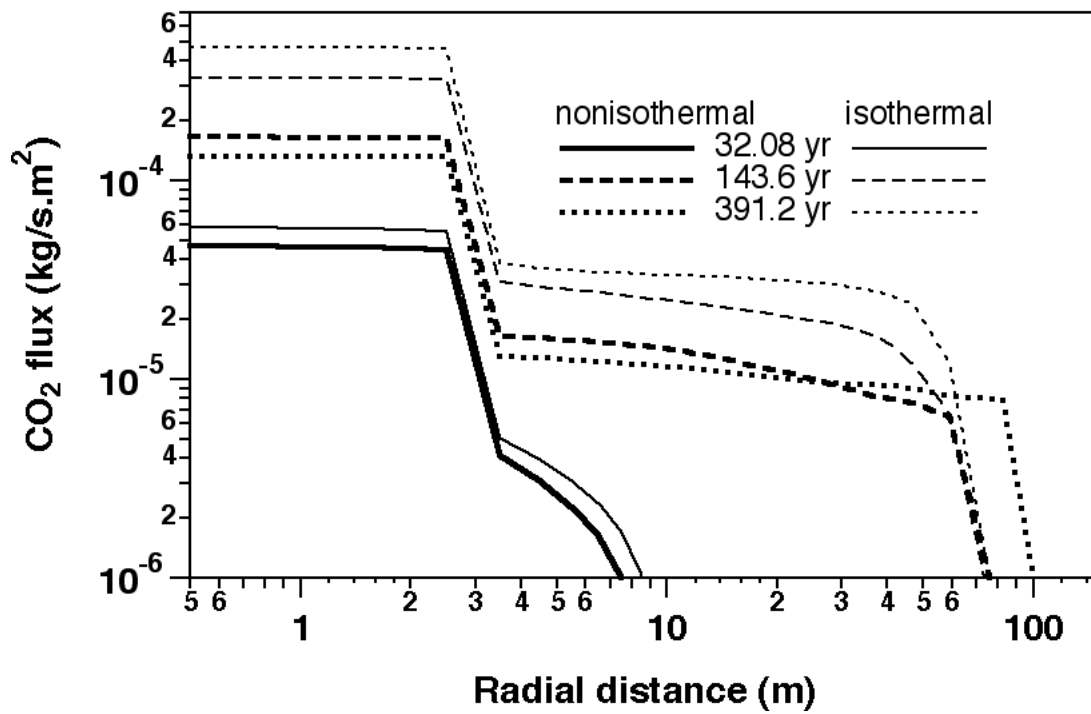


Figure 4.2. Profiles of CO₂ fluxes at the land surface at three different times.

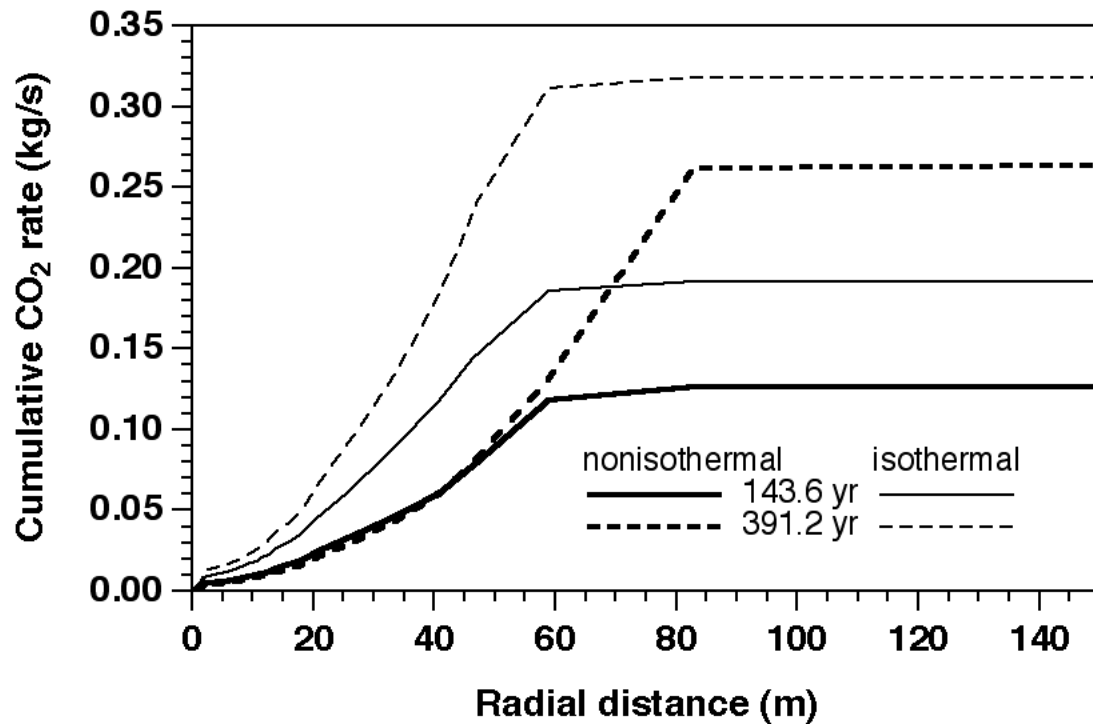


Figure 4.3. Cumulative CO₂ discharge rate, integrated from R = 0 outward, at two different times.

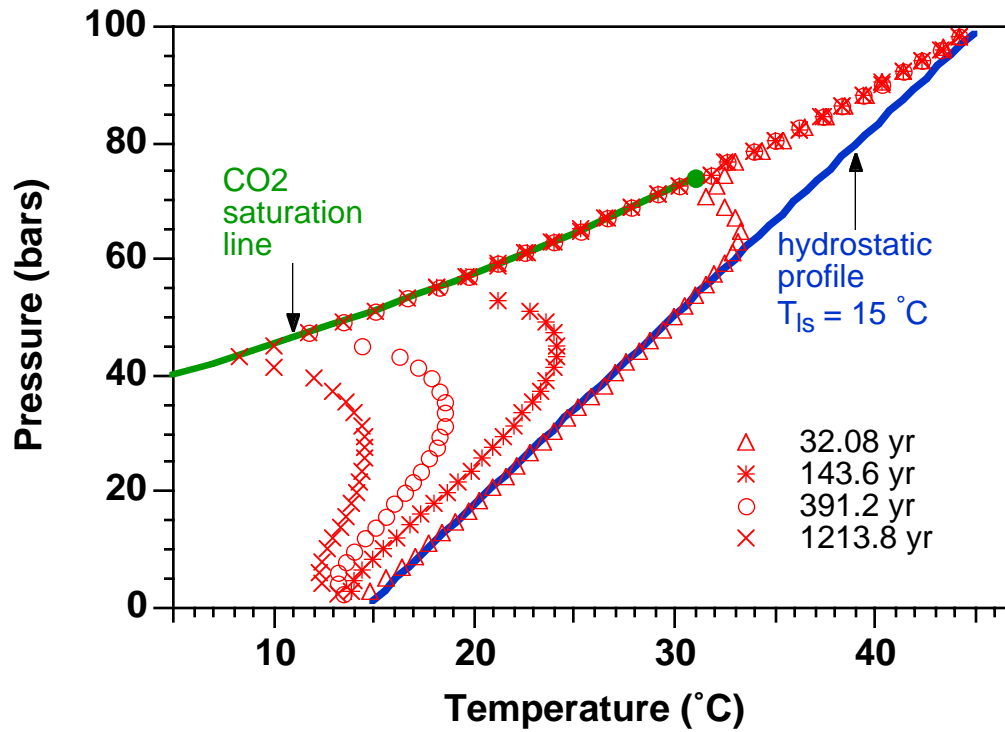


Figure 5.1. Temperature-pressure profiles in the central upflow channel for a case with land surface temperature of 15 °C at different times.